

Tailoring Physical Properties of Crystals through Synthetic Temperature Control: A Case Study for new Polymorphic NbFeTe₂ phases

Hanlin Wu¹, Sheng Li¹, Yan Lyu^{2,3}, Yucheng Guo^{4,5}, Wenhao Liu¹, Ji Seop Oh^{4,6}, Yichen Zhang⁴, Sung-Kwan Mo⁵, Clarina dela Cruz⁷, Robert J. Birgeneau^{4,6}, Keith M. Taddei^{7,*}, Ming Yi^{4,*}, Li Yang^{2,*} and Bing Lv^{1,*}

1 Department of Physics, University of Texas at Dallas, Richardson, TX, 75080, USA

2 Department of Physics and Institute of Materials Science and Engineering, Washington University, St. Louis, MO, 63130, USA

3 Department of Physics, Nanchang University, Nanchang, 330031, China

4 Department of Physics and Astronomy, Rice University, Houston, TX, 77005, USA

5 Advanced Light Source, Lawrence Berkeley National Laboratory, Berkeley, CA, 94720, USA

6 Department of Physics, University of California, Berkeley, CA, 94720, USA

7 Neutron Scattering Division, Oak Ridge National Laboratory, Oak Ridge, TN, 37831, USA

To whom correspondence should be addressed: ktaddei@anl.gov, mingyi@rice.edu, yangli@wustl.edu, blv@utdallas.edu

Abstract

Growth parameters play a significant role in the crystal quality and physical properties of layered materials. Here we present a case study on a van der Waals magnetic NbFeTe₂ material. Two different types of polymorphic NbFeTe₂ phases, synthesized at different temperatures, display significantly different behaviors in crystal symmetry, electronic structure, electrical transport, and magnetism. While the phase synthesized at low temperature showing behavior consistent with previous reports, the new phase synthesized at high temperature, has completely different physical properties, such as metallic resistivity, long-range ferromagnetic order, anomalous Hall effect, negative magnetoresistance, and distinct electronic structures. Neutron diffraction reveals out-of-plane ferromagnetism below 70K, consistent with the electrical transport and magnetic susceptibility studies. Our work suggests that simply tuning synthetic parameters in a controlled manner could be an effective route to alter the physical properties of existing materials potentially unlocking new states of matter, or even discovering new materials.

I. INTRODUCTION

The unique atomically thin 2D van der Waals (*vdW*) structures offer a remarkable platform for investigating the interplay between the spin, charge, orbital, and lattice degrees of freedom. [1–6] They also give rise to new physical phenomena including novel intrinsic magnetism and frustrated magnetism in the 2D atomic limit. The 2D magnetism was first discovered in CrI₃ [7] and Cr₂Ge₂Te₆ [8] despite predictions by the Mermin-Wagner theorem that prohibit long-range magnetic order at finite temperatures in isotropic 2D systems. Furthermore, 2D magnetism has also been achieved in the layered transition metal dichalcogenides (TMDs) such as CrTe₂ [9] and VSe₂ [10]. The combination of electronic structure and magnetism make the TMDs more interesting potentially hosting novel quantum phenomena. [11] The coexistence of multiple stable phases for TMDs with slight differences in the interatomic distance and coordination environment causing significant changes in their physical properties, has been rather appealing, especially for the metastable phases such as the T_d, 1T, 1T' and 1T'' phases. [12–14] Therefore, exploring new 2D *vdW* magnetic materials which are structurally and chemically akin to TMDs, or magnetically intercalating metastable TMD phases, will be a fertile field that could open new research avenues towards emergent phenomena.

In order to discover new phases for intercalated TMDs and new 2D *vdW* magnets, modulating the synthetic parameters such as growth temperatures and fluxes, has been found to be very effective to tune the physical properties and even lead to the discovery of new materials [15–19]. For instance, more than ten unique structural types have been discovered in the ternary copper chalcogenide system by systematically varying the temperature and flux ratios without altering the proportions of starting materials. [20–22] By simply changing the flux and synthetic temperature, new polymorphic BaCu₂As₂ phase with intergrowth feature and new BaCu₆Sn₂As_{4-x} phases are identified in the copper pnictide system. [17,23] Similarly, significant changes of physical properties have been reported in the layered ZrTe₃ crystals synthesized at different temperatures. [18] The low-temperature-synthesized crystals display a charge density wave (CDW) at 70K while high-temperature-synthesized crystals, with atomic disorders at Zr and Te sites, show suppression of CDW order and bulk superconductors at 4K.

NbTe₂ is a non-magnetic 1T' TMD phase, which exhibits the coexistence of CDW order with a transition temperature above 550K and superconductivity below 0.75K. [24–26] In the course of our intercalation studies, where we introduced Fe, Co and Ni ions aiming to induce magnetic orders in this system, we found two distinct NbFeTe₂ phases at different synthetic temperatures, which exhibited drastic changes in crystal symmetry and physical properties. The low-temperature synthesized phase (LT phase) possessed an orthorhombic structure which has been reported previously. [27,28] It can be treated as the interstitial sites filled T_d phase, and the experimental results suggested it is an Anderson insulator with spin glass behavior, consistent with previous studies. [28] The high-temperature synthesized phase (HT phase) crystalizes in a monoclinic crystal structure and displays a clear ferromagnetic order with transition temperature T_c around 70K. Consistent with the ferromagnetic order, a large negative magnetoresistance and anomalous Hall effect are observed in this system. Furthermore, we found that the LT phase can be transformed into the HT phase through simple thermal annealing. Our results demonstrate an effective yet simple approach for examining the effects of synthetic parameters in a controlled manner, which can not only lead to the discovery of new quantum materials, but also provide new insights into their magnetic, transport properties and functionalities of existing materials.

II. EXPERIMENTAL SECTION

Single crystals of both HT and LT NbFeTe₂ were synthesized using the chemical vapor transport method using I₂ as transport agent with the starting materials Nb powder (99.9%, Alfa Aesar), Fe powder (99.99%, Alfa Aesar), and Te lumps (99.999+%, Alfa Aesar). All the synthesis procedures were carried out within a purified Ar-atmosphere glovebox with total O₂ and H₂O levels <0.1 ppm. Chemical stoichiometric elements of Nb, Fe and Te were loaded into the quartz tube with a small amount of I₂ (1 mg/cm³). The quartz tubes were then put into the tube furnace with different temperature profiles. The HT phase with typical size of 3×3×0.2 mm³ were obtained at the source side for two weeks reaction with temperature profile of 1000 °C (source)/900 °C (sink), while the LT phase with typical size of 1×1×0.1 mm³ were obtained for the same two weeks reaction with temperature profile of 750 °C(source)/650 °C (sink). Both crystals are plate-like with shining metallic luster surfaces. Different synthetic parameters have also been tested to figure out the growth windows and optimize the growth conditions for the HT phase. The HT phase could also be synthesized with temperature gradient of 950 °C (source)/850 °C (sink) or 900 °C (source)/800 °C (sink) with prolonged growth time over a month yet with smaller size crystals. In these growth conditions, we did not observe coexisting HT and LT phases. The crystals of LT phase could be converted to HT phase by post-annealing the crystals at 950 °C for a week.

Powder X-ray diffraction (XRD) was performed using a Rigaku Smartlab diffractometer with Cu K_α radiation. Single-crystal X-ray analysis was performed using a Siemens SMART diffractometer equipped with a CCD area detector and monochromatic Mo K_α1 radiation ($\lambda = 0.71073 \text{ \AA}$). The collected dataset was integrated with Bruker SAINT and scaled with Bruker SADABS (multi-scan absorption correction). [29] A starting model was obtained using the direct method in SHELXT [30] and atomic sites were refined anisotropically using SHELXL2014. The composition of all crystals was confirmed by SEM energy-dispersive X-ray spectroscopy (SEM-EDX) using Zeiss EVO LS 15 SEM with accelerating voltage of 20 keV. The data was collected on several crystals with at least five measured points for each crystal to confirm the homogeneity and accurate composition of the crystals. The electrical resistivity, Hall effect and specific heat data was performed in the Quantum Design Physical Property Measurement System (PPMS).

Temperature and field dependent magnetization data was measured on the Quantum Design DynaCool system.

Calculations are performed by using first-principles density functional theory (DFT) with the Perdew–Burke-Ernzerhof (PBE) functional and a kinetic energy cutoff of 400 eV, as implemented in *Vienna Ab initio Simulation Package* (VASP) [31,32]. The first Brillouin zones are sampled with $6 \times 10 \times 8$ k-point meshes. vdW interactions are adopted by the DFT-D3 method [33]. On site Hubbard interaction is adopted by the Dudarev scheme [34], with a range of U from 0 to 3 eV for Fe ions. For geometry optimizations, all atoms are fully relaxed until the residual force per atom is less than 0.01 eV/Å. Spin-orbital coupling (SOC) is included in the calculations.

Neutron powder diffraction (NPD) measurements were performed on the HB-2A powder diffractometer of Oak Ridge National Laboratory’s (ORNL) High Flux Isotope reactor (HFIR) [35]. Patterns were collected between 1.5 and 125 K; and under an applied magnetic field between 0 and 4 T using a cryomagnet. An incident wavelength of 2.41 Å and pre-monochromator, pre-sample and pre-detector collimator settings of open, 21’ and 12’ respectively. Full patterns were collected with 4 hr count times and order parameter-like scans were collected on magnetic Bragg peaks by moving the detector to the relevant 2θ and collecting on warming. Single crystal neutron diffraction data were collected on the WAND² diffractometer of ORNL’s HFIR. Data were collected in the H0L scattering plane between 1.5 and 200 K using a cryostat with a vertically focused incident beam of 1.48 Å. Rietveld refinements were performed using the Fullprof software suite [36]. Representational analysis was performed using SARAh. [37]

ARPES measurements were performed using a Scienta R4000 electron analyzer at Beamline 10.0.1 of the Advanced Light Source (ALS) with an energy resolution and angular resolution of 12 meV and 0.3°, respectively. The samples were cleaved *in-situ* and measured with the base pressure below 4×10^{-11} Torr at 15K.

III. RESULTS AND DISCUSSION

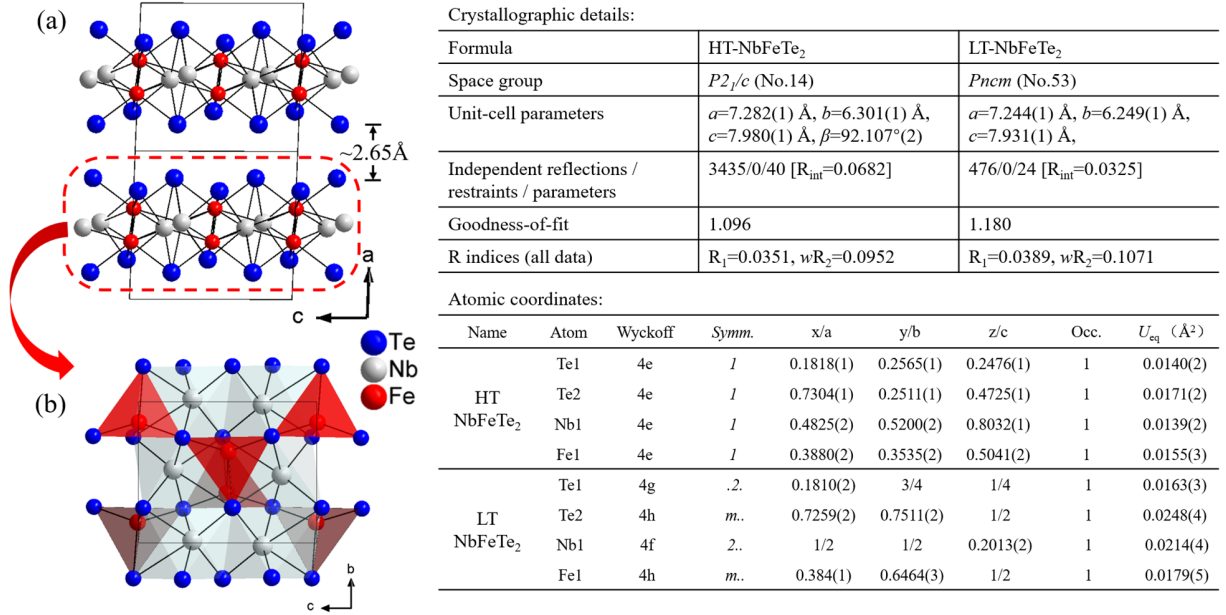


FIG. 1: (a) Crystal structure of HT phase of NbFeTe₂ projected along the *b* direction showing the layered structure; (b) The in-plane NbFeTe₂ layer projected along *a* direction highlighting NbTe₆ octahedra and FeTe₄ tetrahedra in the *bc* plane. (c) Crystal refinement details and atoms coordination for both HT phase and LT phase of NbFeTe₂.

Both HT and LT crystals show only the NbFeTe₂ phase and no other impurity elements present from chemical analysis in SEM-EDX (Fig. S1). However, significant differences in crystal symmetry were observed in X-ray single crystal diffraction. As shown in Fig. 1, both HT and LT phases have layered structures with interlayer distances of ~ 2.65 Å. The layers [Fig. 1(b)] consist of NbTe₆ octahedra, which are face sharing along the *b* axis and edge sharing along *c* axis, with Fe atoms at the interstitial sites forming FeTe₄ tetrahedra. Each Fe atom form a dumbbell-like motif with another Fe atoms, and each dumbbell is connected through extra Te atoms. The LT phase is found in the orthorhombic system with space group *Pnca* (No. 53). The refined unit cell parameters are $a = 7.244(1)$ Å, $b = 6.249(1)$ Å, and $c = 7.931(1)$ Å, which are consistent with previously reported phase [27]. The HT phase crystallizes in the monoclinic system with space group *P2₁/c* (No. 14), and the refined unit cell parameters are $a = 7.282(1)$ Å, $b = 6.301(1)$ Å, and $c = 7.980(1)$ Å and $\beta = 92.11^\circ$. We note that we

intentionally use the non-standard space group *Pnmc* rather than the standard #53 *Pmna* for the refinement so that one can directly compare the difference between the HT and LT phases. The detailed refinement results are shown in Fig. 1(c), with the final CIF files for both compounds provided in the supplemental information. Both phases have two distinct crystallographic sites for Te, one distinct site for Fe and Nb atoms, respectively. Most of the Nb-Te and Fe-Te distances are similar with each other between HT phase and LT phase [2.764(1)- 2.863(1) Å for Nb-Te and 2.551(2)- 2.646(2)Å for Fe-Te], and are similar to bond distances in the Nb₂SiTe₄ (2.845-2.965 Å) [38], NbTe₂ (2.695-2.885Å) [39], Nb₃Sb₂Te₅ (2.894-2.927 Å) [40] and FeTe₂ (2.552- 2.564) Å [41]. The major difference between the two phases lies in the placement of the Nb atom, where it changes from the higher symmetric *4f* site [$\frac{1}{2}$, $\frac{1}{2}$, 0.2013(2)] for the LT phase, to a lower *4e* site [0.4825(4), 0.5200(4), 0.1968(4)]. As such, it causes distortion on the NbTe₆ octahedra where the two Nb-Te₂ distances are changed from 3.278(1) Å in LT phase to 3.012(1) Å and 3.667(2) Å in the HT phase with associated severe Te-Nb-Te angle changes. The 3.667 Å Nb-Te₂ distance suggest non-bonding between the two atoms, and thus cause the more severe distortion on the NbTe₆ octahedra packing, resulting in the broken structural symmetry and its transformation from orthorhombic in LT phase to monoclinic HT phase.

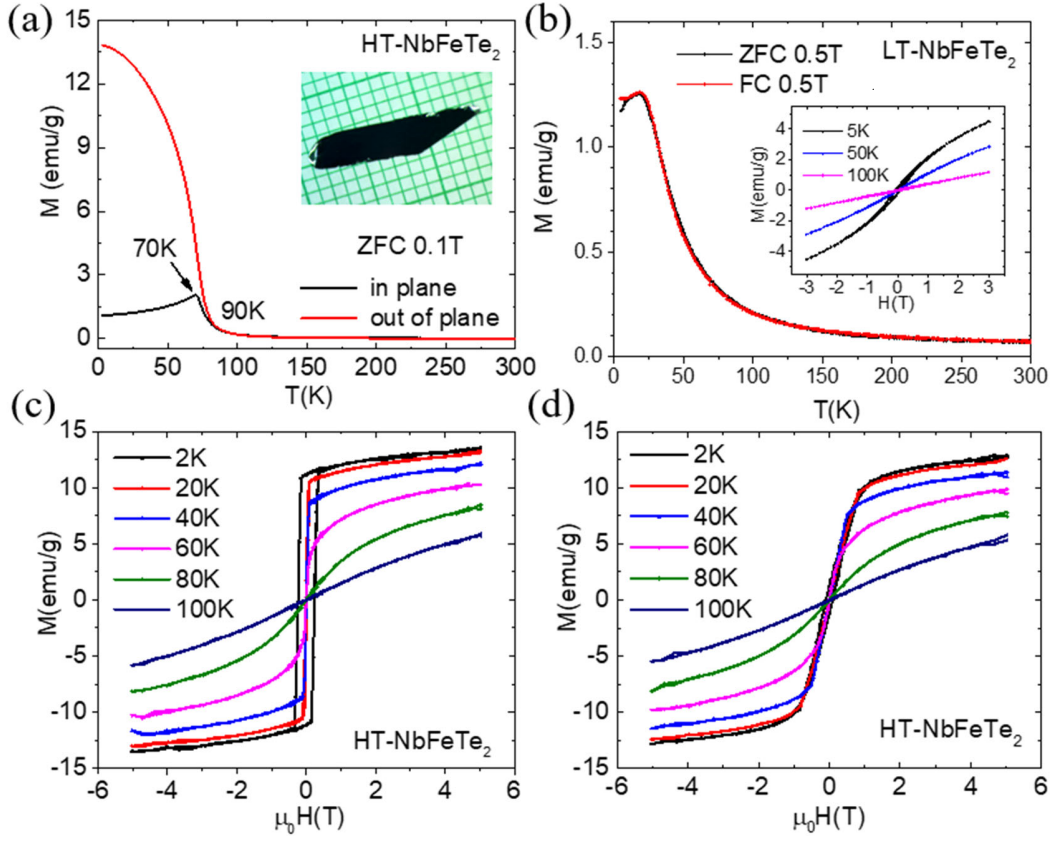


FIG. 2: (a) Temperature dependent of magnetization with magnetic field along and perpendicular to crystal plane under magnetic field 0.1T for HT NbFeTe₂. Inset is the image of single crystal of HT NbFeTe₂ on a millimeter-scale sheet. (b) Temperature dependent of magnetization of LT NbFeTe₂. Inset is magnetic hysteresis loops at different temperature. Isothermal magnetic hysteresis loops of HT NbFeTe₂ with field direction (c) perpendicular and (d) parallel to the crystal layers.

To explore the influence of the structural difference between HT phase and LT phase, we investigate the magnetic and transport properties, and surprisingly find that these two phases show completely different behaviors. Temperature dependent magnetization of HT phase is shown in Fig. 2(a). By applying a magnetic field along different orientation, we observe a distinct magnetization behavior for HT phase, where a typical FM behavior with magnetic field perpendicular to the layer and a cusp at 70K with magnetic field parallel to the layer. Such behavior is also observed in other layered magnets which indicate the magnetic moment is perpendicular to the layer. [42,43] The magnetization curves overlap

above 90K, and the splitting of magnetization between T_c and 90K suggests strong spin fluctuations within this temperature range. The LT phase, clearly show no magnetic order at high temperature with a spin glass magnetic transition occurred at low temperature (~ 15 K) [Fig. 2(b)]. This is consistent with the previous report [28].

By applying a magnetic field perpendicular and parallel to the layer direction of HT phase, magnetic anisotropic behaviors are observed as shown in Fig. 2(c) and 2(d). Based on the magnetization hysteresis (MH) loops at different temperatures, the a -axis is recognized as the easy axis for magnetization, because the saturation field along $H // a$ ($H^a \sim 3.5$ kOe) is far below that of $H // bc$ ($H^{bc} \sim 13$ kOe). This anisotropy is further highlighted by the difference in saturated magnetic moments calculated from Fig. 2(c) and 2(d), which are estimated to be $\mu_s^a = 0.95\mu_B$ and $\mu_s^{bc} = 0.89\mu_B$. Additionally, the nonlinear magnetization loops observed at 80K in both directions are consistent with temperature dependent magnetization in Fig. 2(a), which are likely due to strong spin fluctuations.

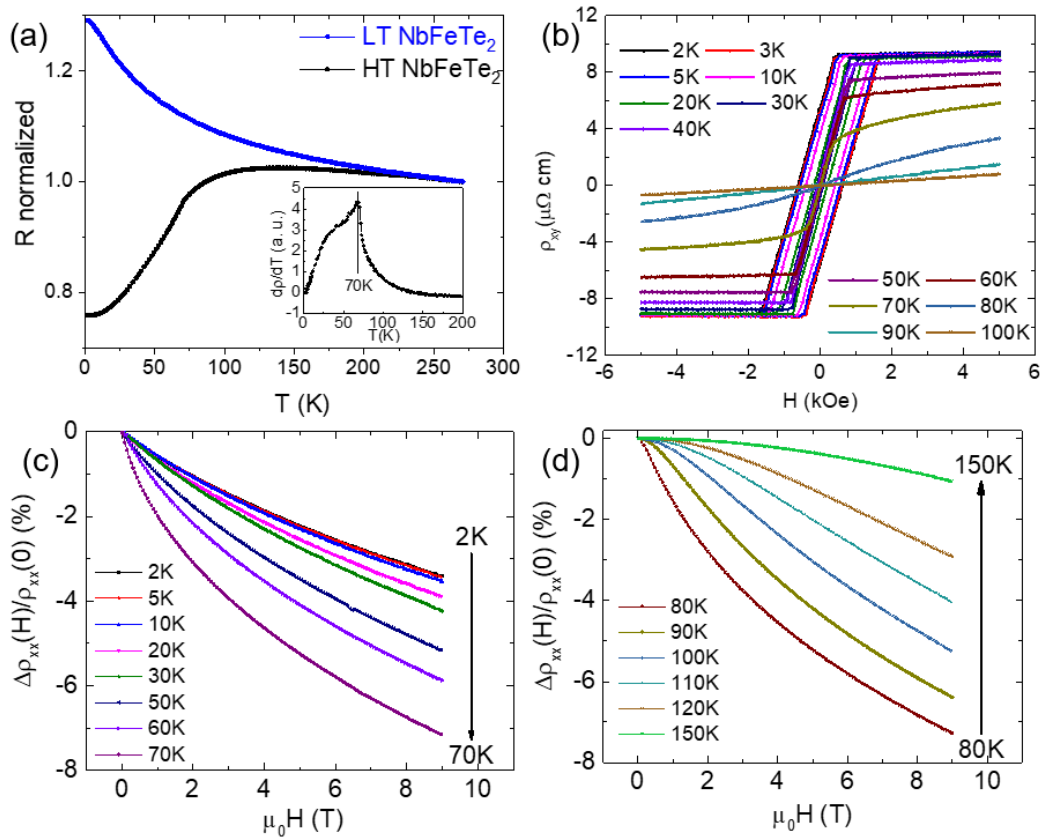


FIG. 3: (a) Temperature dependent normalized resistivity data of LT and HT NbFeTe₂. Insert is first derivative of HT resistivity curve. (b) Hall resistivity of HT NbFeTe₂ at different temperature. Magnetoresistance of HT NbFeTe₂ at (c) 2-70 K and (d) 80-150 K.

Besides the LT and HT phases exhibiting different magnetic ground states, the electrical properties also show distinct behaviors between the two phases. Temperature dependent resistivity data for the HT and LT phases are shown in Fig. 3(a). Consistent with previous results, the resistivity of the LT phase shows a semiconducting trend at low temperature due to the strong localization, resulting in the LT phase likely being an Anderson insulator. The Anderson localization may arise from the small Fe vacancies [44]. Resistivity of the HT phase increases slightly as temperature decreases at first, and then decreases with further decreasing of the temperature, showing a metallic ground state. A broad peak at 70K in the first derivative of the resistivity data [inset of Fig. 3(a)] is observed, consistent with the magnetic transition of HT phase at 70K. To exclude that the FM transition and resistivity anomaly in the HT phase originates from a structural transition, we performed both temperature dependent single crystal diffraction down to 80K and Neutron diffraction at low temperature (discussed later), and no such transition is observed. This anomaly might be associated with a Lifshitz transition, similar to that of ZrTe₅ [45,46]. We indeed observe an anomalous Hall effect (AHE) up to 80 K in Fig. 3(b) for the HT phase, which slightly exceeds the FM transition temperature at 75K but is consistent with our suggestions of strong spin fluctuations persisting up to ~90 K from magnetic anisotropic measurements. We then investigate magnetoresistance (MR) for the HT phase at different temperatures. A large negative MR (nMR) is observed from 2K to 150K as shown in Fig. 3(c) and 3(d). The nMR curvature follows parabolic behaviors, where the MR value at 9T first increases and then decreases as the temperature increases. A crossover of nMR at ~ 70K is observed, which corresponds to the FM transition and could be attributed to the electron scattering by strong spin fluctuations near the magnetic transition [47].

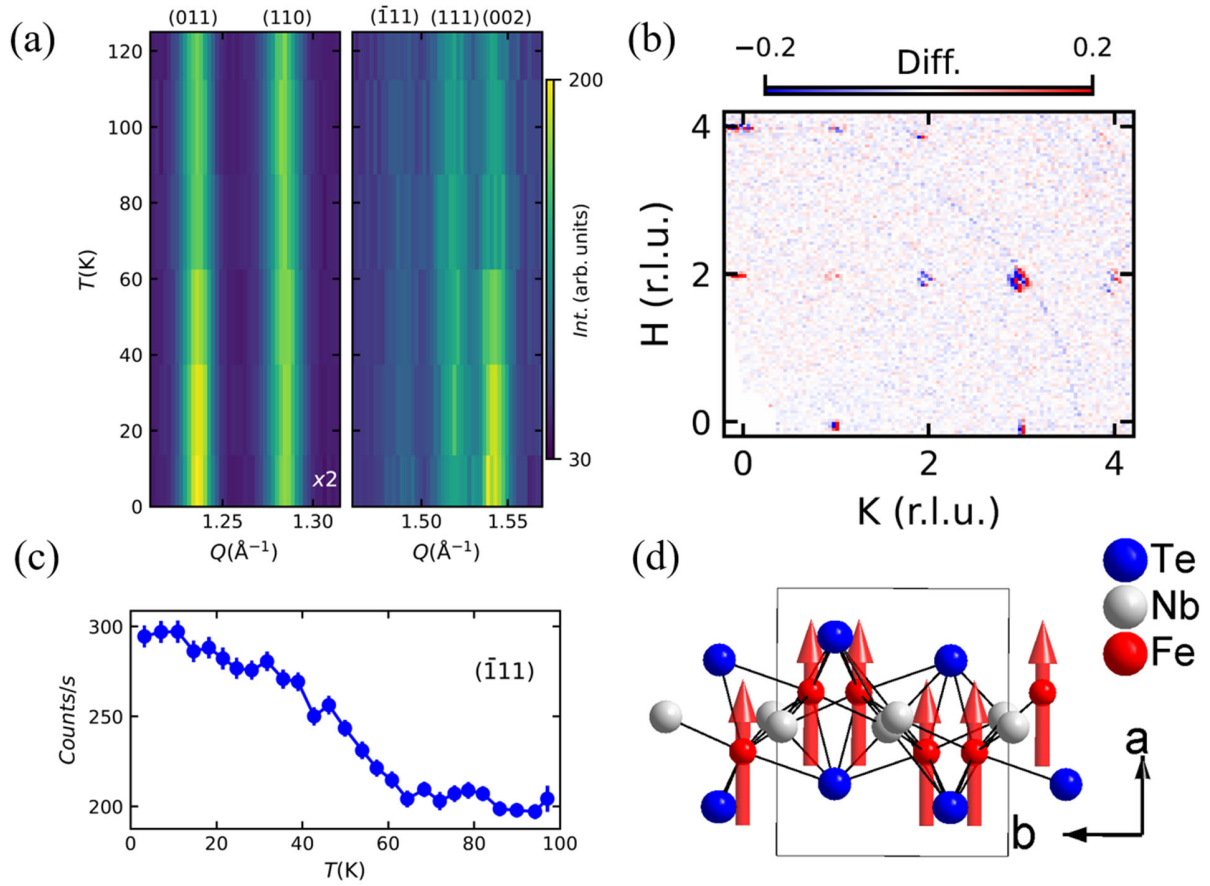


FIG. 4: (a) Neutron powder diffractogram of HT NbFeTe_2 . (b) Order parameter scan collected while warming the sample. (c) Difference plot of low (10 K) and high (100 K) neutron scattering intensities of a single crystal sample. (d) Magnetic structure determined from representational analysis using neutron diffraction data.

To unambiguously elucidate the magnetic order in the HT NbFeTe_2 phase, we perform NPD measurements. NPD patterns and best fit models from Rietveld refinements for data for 125K and 2K are shown in supplemental Fig. S2. In Fig. 4(a), temperature dependent neutron powder diffractogram shows the scattering intensity for a series of low Q peaks at low temperatures. Here a change in scattering intensity is clearly seen which coincides with the signal at 70K, observed in both the magnetization and resistivity measurements. As no such intensity change is observed in the XRD we attribute the scattering to a magnetic origin. To better characterize the transition, we collect the intensity of the $\bar{1}11$ peak as a function of temperature upon warming [Fig. 4(b)]. The peak intensity increases with decreasing temperature when

temperature is below 70K. The $\bar{1}11$ peak is chosen due to its seemingly minimal contribution from nuclear scattering as seen in its nearly becoming background equivalent about 70 K in Fig. 4(a). To carefully check for any weak additional magnetic scattering and help discriminate between potential magnetic symmetries, single crystal neutron diffraction is collected in the (H 0 L) plane at 10K and 100 K and then plotted as a difference map in Fig. 4(c). As seen, there is some difference in the intensities seen at integer positions, which is consistent with FM ordering, but no additional scattering is observed. With this information, magnetic structure solution is performed using representational analysis to consider all potential magnetic structures allowed by a ferromagnetic $k=000$ ordering vector, the Wyckoff position of the Fe site and the crystallographic space group, as shown in Table S1. Of the potential magnetic structures, the best fit model was found to have purely ferromagnetic components along a axis can be characterized via representational analysis as the Γ_3 irreducible representation of the nuclear space group and the (0,0,0) ordering vector, which corresponds to the magnetic space group $P2'_1/c'$, as shown in Fig. S2. In Fig. 4(d), the magnetic structure is shown with all the Fe magnetic moments along a axis as expected from the temperature dependent magnetization measurement in Fig. 2a. The refined magnetic moment of Fe is $0.4 \mu_B$, which is smaller than the value estimated from magnetic measurements and can be consistent with itinerant ferromagnetism as seen in systems such as Fe_3GeTe_2 . [48] We note that although our solution only contains a moment component along a , this is not an explicit constraint of the Γ_3 irrep. As shown in table S1, Γ_3 has three basis vectors, one each for the three crystallographic directions. In our analysis, the best fit was produced with a model where only the basis vector describing a FM moment along a was allowed to have a non-zero contribution. None the less, as the moment is allowed by symmetry to have non-zero components along b and c we cannot completely rule them out. However, we can put an upper limit on their value based on the sensitivity of our NPD measurements at $< 0.1 \mu_B$. Additional measurements were performed under an applied field under both field cooled (FC) and zero-field cooled (ZFC) procedures. No additional peaks nor meaningful change in the peak intensities was observed indicating the absence of a metamagnetic transition up to 4 T.

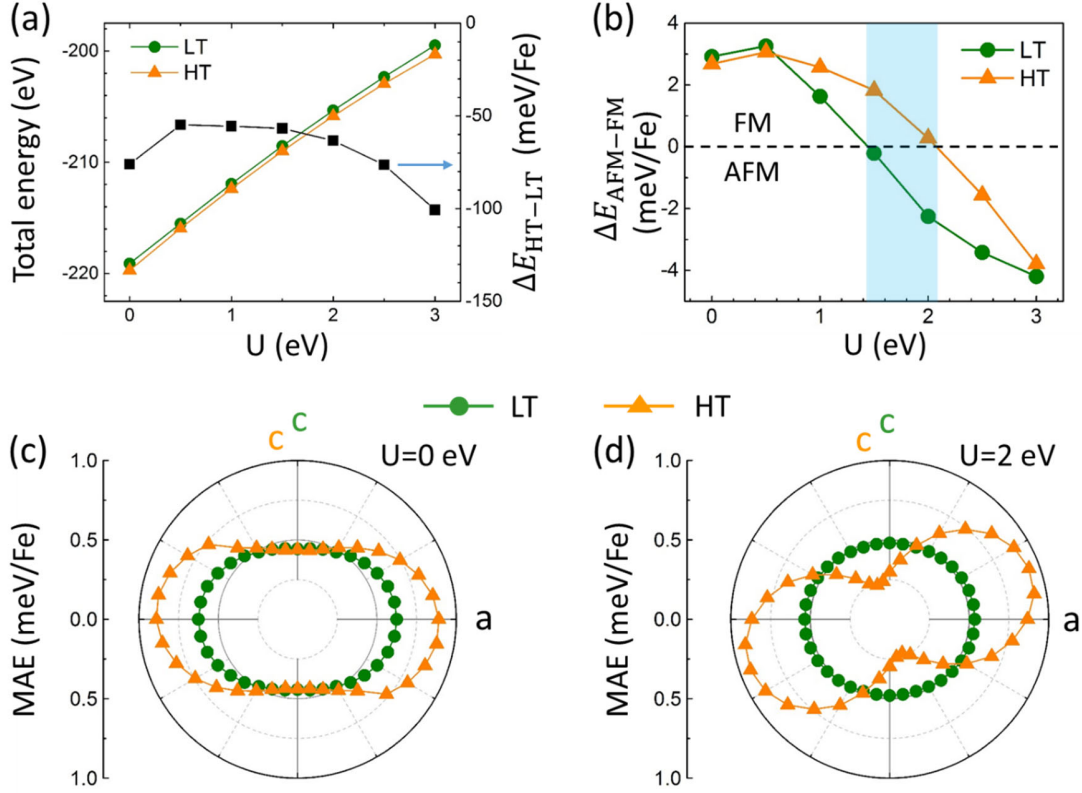


FIG. 5: (a) DFT-calculated total energy and energy difference between LT and HT NbFeTe₂. (b) Interlayer coupling as a function of U of Fe ions. Magnetic anisotropic energy in the ac plane for LT and HT NbFeTe₂, calculated by (c) $U=0$ eV and (d) $U=2$ eV.

To fully understand the experimental results, we investigate the electronic and magnetic states of HT and LT phases of NbFeTe₂ by using DFT calculations. The energy bands and projected density of states calculated by DFT+ U with different U value are shown in Fig. S3 and S4. As shown in Fig. 5(a), the HT phase has lower total energies than the LT phase, which is about 50-100 meV/Fe lower in the range of 0-3 eV of the value of Hubbard interaction (U) of Fe ions. This supports the observation that LT phase can transfer to HT phase by thermal annealing process. The local magnetic moments are found mostly from the Fe ions. For example, the magnetic moments of Fe and Nb ions are 2.55 and $-0.32 \mu_B$, respectively, calculated by $U = 2.0$ eV for Fe ions. Calculations of possible magnetic states suggest that the ground state of intralayer magnetic coupling is FM between Fe ions and AFM between Fe and Nb ions for both LT and HT phases. These intralayer coupling states are strong and robust with respect to different values of U . On

the other hand, the ground state of interlayer coupling is sensitive to the value of U of Fe ions, as shown in Fig. 5(b), where the critical values of U for interlayer FM/AFM transition are different for LT and HT phases. In the range of 1.4-2.1 eV of U , the LT phase is interlayer AFM, while the HT phase is interlayer FM, which agrees with the measured FM state of the HT phase.

To explain the different magnetic orders of HT and LT phases, the magnetic anisotropic energy (MAE) with different values of U is calculated and plotted in Figs. 5(c) and 5(d). The magnetic easy axis is nearly along the out-of-plane direction (the a axis) for both HT and LT phases. However, when comparing in-plane directions (along c axis) with $U=0$ eV, the HT phase is more anisotropic than the LT phase [Fig. 5(c)]. And as increasing value of U to 2 eV, the LT phase becomes more isotropic, while the HT phase becomes more anisotropic in the ac plane [Fig. 5(d)]. As it is believed that MAE is necessary to induce the long-range magnetic orders in layered magnetic materials at finite temperature [8], the significant MAE may contribute to the observed FM order in the HT phase while the nearly isotropic MAE in the LT phase may result in the spin glass state, instead of the long-range order.

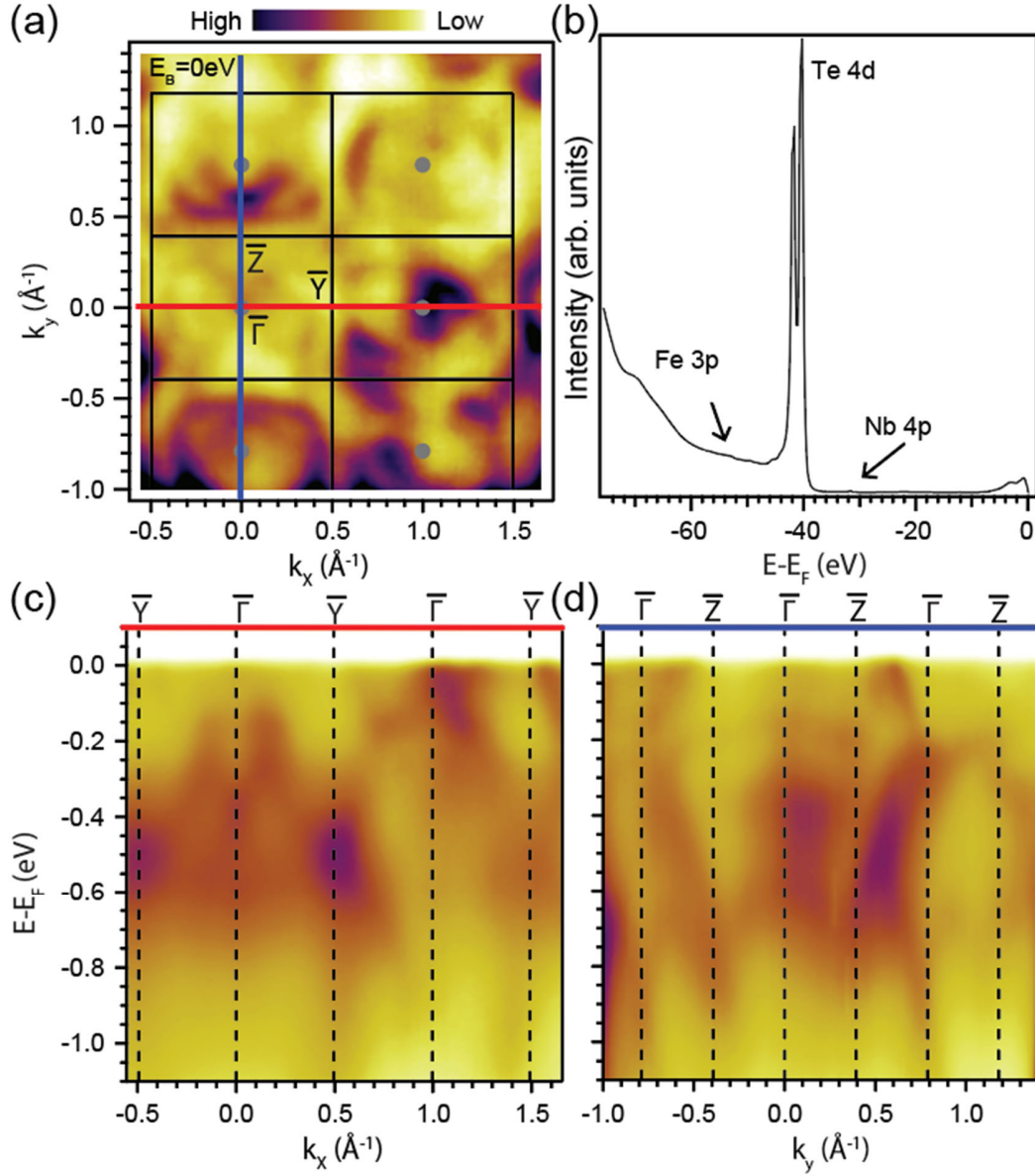


FIG. 6: (a) Fermi Surface of HT NbFeTe₂. The Brillouin zones are labeled in black. (b) Experimental angle-integrated photoemission spectra. (c) Band dispersions along \bar{Y} - $\bar{\Gamma}$ - \bar{Y} , denoted by the red line in (a). (d) Band dispersions along \bar{Z} - $\bar{\Gamma}$ - \bar{Z} , denoted by the blue line in (a). All measurements were performed with 78 eV photons at 15K.

To investigate the electronic structure, we have carried out ARPES measurements of HT NbFeTe₂ in the FM state (Fig. 6). Fermi surface map in Fig. 6(a) demonstrates pronounced matrix element effects,

which are further revealed in the band dispersions along the high symmetry directions in Fig. 6(c)-(d). In the cuts, the band dispersions along $\bar{Z}-\bar{\Gamma}$ (or $\bar{Y}-\bar{\Gamma}$) are normally expected to be identical with the band dispersion along the same cut in different Brillouin zones due to the translational symmetry of the lattice. Here, however, the bands exhibit significant intensity variations due to the strong photoemission matrix element effect. Its origin needs further investigation. The core levels in the angle-integrated photoemission spectra in [Fig. 6(b)] confirms the existence of Tellurium, Niobium, and Iron in the compound. The dispersive bands at the Fermi level suggests the system is metallic in the FM state. This observation is consistent with the electrical transport results and stands in stark contrast to the LT NbFeTe₂ where flat bands emerge at the Fermi level due to Anderson localization and result into an insulating behavior in the electrical transport measurements [28].

IV. CONCLUSION

In conclusion, we have presented a case study on discovery of a high-temperature polymorphic phase of layered NbFeTe₂ by simply modifying the synthetic temperatures. Compared to previously reported NbFeTe₂ with spin glass transition, this new polymorphic HT NbFeTe₂ phase has lower crystal symmetry and shows completely different physical properties. Electrical transport, magnetic susceptibility and Neutron diffraction studies show a clear long range out-of-plane ferromagnetic transition at 70K. ARPES study confirm a metallic electronic structure in the FM state. HT NbFeTe₂ also displays a metallic behavior with negative MR over the whole temperature range, and AHE occurs below ferromagnetic transition temperature. The electronic and magnetic states of two different phases of NbFeTe₂ have been investigated while the simulation results agree with the measurements. The first-principles calculation suggests that the variation of MAE could be the origin for observed different magnetic orderings in LT and HT phases. It appears that synthetic parameters by both ex-situ temperatures/post-annealing or in-situ synthesis/diffraction combination in a controlled manner could be fruitful directions to explore for materials discovery in the future.

Acknowledgements:

This work at the University of Texas at Dallas is supported by the US Air Force Office of Scientific Research (AFOSR) Grant no. FA9550-19-1-0037, National Science Foundation (NSF) (DMREF-1921581) and Office of Naval Research (ONR) grant no. N00014-23-1-2020. Part of our measurement facilities acknowledge the support from the AFOSR Defense University Research Instrumentation Program (DURIP) grant no. FA9550-21-1-0297. The ARPES work at Rice University was supported by the Robert A. Welch Foundation Grant No. C-2175 and the Gordon and Betty Moore Foundation's EPiQS Initiative through grant No. GBMF9470. This research used resources of the Advanced Light Source, which is a DOE Office of Science User Facility under contract no. DE-AC02-05(c)H11231. Yucheng Guo was supported in part by an ALS Doctoral Fellowship in Residence. L.Y. is supported by NSF DMREF DMR-2118779. The simulation used Anvil at Purdue University through allocation DMR100005 from the Advanced Cyberinfrastructure Coordination Ecosystem: Services & Support (ACCESS) program, which is supported by National Science Foundation grants #2138259, #2138286, #2138307, #2137603, and #2138296. A portion of this research used resources at the High Flux Isotope Reactor, a DOE Office of Science User Facility operated by the Oak Ridge National Laboratory.

Author Information

Keith M. Taddei: ORCID 0000-0002-1468-0823

Sung-Kwan Mo: ORCID 0000-0003-0711-8514

Yichen Zhang: ORCID 0000-0001-6792-330x

REFERENCE

- [1] K. F. Mak, J. Shan, and D. C. Ralph, *Probing and Controlling Magnetic States in 2D Layered Magnetic Materials*, Nat. Rev. Phys. **1**, 646 (2019).
- [2] P. Huang, P. Zhang, S. Xu, H. Wang, X. Zhang, and H. Zhang, *Recent Advances in Two-Dimensional Ferromagnetism: Materials Synthesis, Physical Properties and Device Applications*, Nanoscale **12**, 2309 (2020).
- [3] S. Rahman, J. F. Torres, A. R. Khan, and Y. Lu, *Recent Developments in van Der Waals Antiferromagnetic 2D Materials: Synthesis, Characterization, and Device Implementation*, ACS Nano **15**, 17175 (2021).
- [4] Z. Zhao, W. Li, Y. Zeng, X. Huang, C. Yun, B. Zhang, and Y. Hou, *Structure Engineering of 2D Materials toward Magnetism Modulation*, Small Struct. **2**, 2100077 (2021).
- [5] S. Xing, J. Zhou, X. Zhang, S. Elliott, and Z. Sun, *Theory, Properties and Engineering of 2D Magnetic Materials*, Prog. Mater. Sci. 101036 (2022).
- [6] D. L. Cortie, G. L. Causer, K. C. Rule, H. Fritzsche, W. Kreuzpaintner, and F. Klose, *Two-dimensional Magnets: Forgotten History and Recent Progress towards Spintronic Applications*, Adv. Funct. Mater. **30**, 1901414 (2020).
- [7] B. Huang et al., *Layer-Dependent Ferromagnetism in a van Der Waals Crystal down to the Monolayer Limit*, Nature **546**, 270 (2017).
- [8] C. Gong et al., *Discovery of Intrinsic Ferromagnetism in Two-Dimensional van Der Waals Crystals*, Nature **546**, 265 (2017).
- [9] X. Zhang, Q. Lu, W. Liu, W. Niu, J. Sun, J. Cook, M. Vaninger, P. F. Miceli, D. J. Singh, and S.-W. Lian, *Room-Temperature Intrinsic Ferromagnetism in Epitaxial CrTe₂ Ultrathin Films*, Nat. Commun. **12**, 2492 (2021).
- [10] M. Bonilla, S. Kolekar, Y. Ma, H. C. Diaz, V. Kalappattil, R. Das, T. Eggers, H. R. Gutierrez, M. H. Phan, and M. Batzill, *Strong Roomerature Ferromagnetism in VSe₂ Monolayers on van Der Waals Substrates*, Nat. Nanotechnol. **13**, 289 (2018).
- [11] T. Chowdhury, E. C. Sadler, and T. J. Kempa, *Progress and Prospects in Transition-Metal Dichalcogenide Research beyond 2D*, Chem. Rev. **120**, 12563 (2020).
- [12] S. Tang, C. Zhang, D. Wong, Z. Pedramrazi, H.-Z. Tsai, C. Jia, B. Moritz, M. Claassen, H. Ryu, and S. Kahn, *Quantum Spin Hall State in Monolayer 1T'-WTe₂*, Nat. Phys. **13**, 683 (2017).
- [13] J. Augustin, V. Eyert, T. Böker, W. Frentrup, H. Dwelk, C. Janowitz, and R. Manzke, *Electronic Band Structure of the Layered Compound T_d-WTe₂*, Phys. Rev. B **62**, 10812 (2000).
- [14] C. Shang, Y. Q. Fang, Q. Zhang, N. Z. Wang, Y. F. Wang, Z. Liu, B. Lei, F. B. Meng, L. K. Ma, and T. Wu, *Superconductivity in the Metastable 1T' and 1T'' phases of MoS₂ Crystals*, Phys. Rev. B **98**, 184513 (2018).
- [15] J. S. Kim, E. G. Kim, and G. R. Stewart, *Specific Heat Anomalies for in Superconducting Single Crystal Doped BaFe₂As₂: Comparison of Different Flux Growth Methods*, J. Phys. Condens. Matter **21**, 252201 (2009).
- [16] T. A. Empante, Y. Zhou, V. Klee, A. E. Nguyen, I.-H. Lu, M. D. Valentin, S. A. Naghibi Alvillar, E. Preciado, A. J. Berges, and C. S. Merida, *Chemical Vapor Deposition Growth of Few-Layer MoTe₂ in the 2H, 1T', and 1T Phases: Tunable Properties of MoTe₂ Films*, ACS Nano **11**, 900 (2017).
- [17] H. Wu, S. Li, Z. Wu, X. Wang, G. A. Ofenstein, S. Kwon, M. J. Kim, P. C. W. Chu, and B. Lv, *Novel Polymorphic Phase of BaCu₂As₂: Impact of Flux for New Phase Formation in Crystal Growth*, Cryst. Growth Des. **20**, 5922 (2020).
- [18] X. Zhu, B. Lv, F. Wei, Y. Xue, B. Lorenz, L. Deng, Y. Sun, and C.-W. Chu, *Disorder-Induced Bulk Superconductivity in ZrTe₃ Single Crystals via Growth Control*, Phys. Rev. B **87**, 24508 (2013).
- [19] W. Liu, S. Li, H. Wu, N. Dhale, P. Koirala, and B. Lv, *Enhanced Superconductivity in the Se-Substituted 1T-PdTe₂*, Phys. Rev. Mater. **5**, 14802 (2021).

- [20] V. K. Anand, P. K. Perera, A. Pandey, R. J. Goetsch, A. Kreyssig, and D. C. Johnston, *Crystal Growth and Physical Properties of SrCu₂As₂, SrCu₂Sb₂, and BaCu₂Sb₂*, Phys. Rev. B **85**, 214523 (2012).
- [21] M. Pfisterer and G. Nagorsen, *Zur Struktur Ternärer Übergangsmetallarsenide/On the Structure of Ternary Arsenides*, Zeitschrift Für Naturforsch. B **35**, 703 (1980).
- [22] J. Dünner, A. Mewis, M. Roepke, and G. Michels, *Neue Ternäre Kupferpnictide Mit Modifizierten BaAl₄-Strukturen*, ZAAC - J. Inorg. Gen. Chem. **621**, 1523 (1995).
- [23] H. Wu, S. Li, X. Wang, S. Kwon, W. Liu, G. A. Ofenstein, M. J. Kim, and B. Lv, *New Layered Quaternary BaCu₆Sn₂As_{4-x} and BaCu₆Sn₂P_{4-x} Phases: Crystal Growth and Physical Properties*, J. Alloys Compd. **892**, 162111 (2022).
- [24] M. H. Van Maaren and G. M. Schaeffer, *Some New Superconducting Group Va Dichalcogenides*, Phys. Lett. A **24**, 645 (1967).
- [25] K. Selte and A. Kjekshus, *On the Magnetic Properties of Niobium Selenides and Tellurides*, Acta Chem. Scand **19**, (1965).
- [26] S. Nagata, T. Abe, S. Ebisu, Y. Ishihara, and K. Tsutsumi, *Superconductivity in the Metallic Layered Compound NbTe₂*, J. Phys. Chem. Solids **54**, 895 (1993).
- [27] J. Li, M. E. Badding, and F. J. DiSalvo, *New Layered Ternary Niobium Tellurides: Synthesis, Structure, and Properties of Niobium Metal Telluride, NbMTe₂ (M = Iron, Cobalt)*, Inorg. Chem. **31**, 1050 (1992).
- [28] W. Bai, Z. Hu, S. Wang, Y. Hua, Z. Sun, C. Xiao, and Y. Xie, *Intrinsic Negative Magnetoresistance in van Der Waals FeNbTe₂ Single Crystals*, Adv. Mater. **31**, 1900246 (2019).
- [29] L. Krause, R. Herbst-Irmer, G. M. Sheldrick, and D. Stalke, *Comparison of Silver and Molybdenum Microfocus X-Ray Sources for Single-Crystal Structure Determination*, J. Appl. Crystallogr. **48**, 3 (2015).
- [30] G. M. Sheldrick, *SHELXT—Integrated Space-Group and Crystal-Structure Determination*, Acta Crystallogr. Sect. A Found. Adv. **71**, 3 (2015).
- [31] G. Kresse and J. Furthmüller, *Efficient Iterative Schemes for Ab Initio Total-Energy Calculations Using a Plane-Wave Basis Set*, Phys. Rev. B **54**, 11169 (1996).
- [32] G. Kresse and D. Joubert, *From Ultrasoft Pseudopotentials to the Projector Augmented-Wave Method*, Phys. Rev. B **59**, 1758 (1999).
- [33] S. Grimme, J. Antony, S. Ehrlich, and H. Krieg, *A Consistent and Accurate Ab Initio Parametrization of Density Functional Dispersion Correction (DFT-D) for the 94 Elements H-Pu*, J. Chem. Phys. **132**, 154104 (2010).
- [34] S. L. Dudarev, G. A. Botton, S. Y. Savrasov, C. J. Humphreys, and A. P. Sutton, *Electron-Energy-Loss Spectra and the Structural Stability of Nickel Oxide: An LSDA+ U Study*, Phys. Rev. B **57**, 1505 (1998).
- [35] S. Calder, K. An, R. Boehler, C. R. Dela Cruz, M. D. Frontzek, M. Guthrie, B. Haberl, A. Huq, S. A. J. Kimber, J. Liu, J. J. Molaison, J. Neuefeind, K. Page, A. M. dos Santos, K. M. Taddei, C. Tulk and M. G. Tucker, *A Suite-Level Review of the Neutron Powder Diffraction Instruments at Oak Ridge National Laboratory*, Rev. Sci. Instrum. **89**, 92701 (2018).
- [36] J. Rodríguez-Carvajal, *Recent Advances in Magnetic Structure Determination by Neutron Powder Diffraction*, Phys. B Condens. Matter **192**, 55 (1993).
- [37] A. S. Wills, *A New Protocol for the Determination of Magnetic Structures Using Simulated Annealing and Representational Analysis (SARAh)*, Phys. B Condens. Matter **276**, 680 (2000).
- [38] L. Monconduit, M. Evain, R. Brec, J. Rouxel, and E. Canadell, *Synthesis, Crystal and Electronic Structure of a New Ternary Layered Compound: Nb₂SiTe₄*, Comptes Rendus l'Académie Des Sci. Série 2, Mécanique, Phys. Chim. Sci. l'univers, Sci. La Terre **316**, 25 (1993).
- [39] B. E. Brown, *The Crystal Structures of NbTe₂ and TaTe₂*, Acta Crystallogr. **20**, 264 (1966).
- [40] P. Jensen and A. Kjekshus, *The Crystal Structure of Nb₃Sb₂Te₅*, J. Less Common Met. **13**, 357 (1967).

- [41] G. Brostigen and A. Kjekshus, *Compounds with the Marcasite Type Crystal Structure*, Acta Chem Scand **24**, 1925 (1970).
- [42] X. Zhang, Y. Zhao, Q. Song, S. Jia, J. Shi, and W. Han, *Magnetic Anisotropy of the Single-Crystalline Ferromagnetic Insulator $Cr_2Ge_2Te_6$* , Jpn. J. Appl. Phys. **55**, 33001 (2016).
- [43] G. Zhang, F. Guo, H. Wu, X. Wen, L. Yang, W. Jin, W. Zhang, and H. Chang, *Above-Room-Temperature Strong Intrinsic Ferromagnetism in 2D van Der Waals Fe_3GeTe_2 with Large Perpendicular Magnetic Anisotropy*, Nat. Commun. **13**, 5067 (2022).
- [44] J. Neuhausen, K. Stork, E. Potthoff und W. Tremel, *Synthesis and Structure of $Nb_{0.89}Fe_{0.93}Te_2$ and $Ta_{0.77}Fe_{0.90}Te_2$* Z. Naturforsch. 47b, 1203- 1212 (1992).
- [45] Y. Zhang, C. Wang, L. Yu, G. Liu, A. Liang, J. Huang, S. Nie, X. Sun, Y. Zhang, and B. Shen, *Electronic Evidence of Temperature-Induced Lifshitz Transition and Topological Nature in $ZrTe_5$* , Nat. Commun. **8**, 15512 (2017).
- [46] Q. Li, D. E. Kharzeev, C. Zhang, Y. Huang, I. Pletikosić, A. V Fedorov, R. D. Zhong, J. A. Schneeloch, G. D. Gu, and T. Valla, *Chiral Magnetic Effect in $ZrTe_5$* , Nat. Phys. **12**, 550 (2016).
- [47] M. R. Oliver, J. O. Dimmock, A. L. McWhorter, and T. B. Reed, *Conductivity Studies in Europium Oxide*, Phys. Rev. B **5**, 1078 (1972).
- [48] V. Y. Verchenko, A. A. Tsirlin, A. V Sobolev, I. A. Presniakov, and A. V Shevelkov, *Ferromagnetic Order, Strong Magnetocrystalline Anisotropy, and Magnetocaloric Effect in the Layered Telluride $Fe_{3-x}GeTe_2$* , Inorg. Chem. **54**, 8598 (2015).